


 CrossMark
click for updates

 Cite this: *CrystEngComm*, 2015, 17, 6972

A comprehensive study on the mechanism behind formation and depletion of $\text{Cu}_2\text{ZnSnS}_4$ (CZTS) phases†

 Rameez Ahmad,^a Marco Brandl,^b Monica Distaso,^a Patrick Herre,^{ac} Erdmann Spiecker,^c Rainer Hock^b and Wolfgang Peukert^{*a}

High efficiency kesterite based solar cells have vigorously raised the research interests in this material. The challenge lies in understanding the formation and co-existence of more than 10 possible by-products during and after the synthesis of $\text{Cu}_2\text{ZnSnS}_4$ (CZTS) and their various different structural and electronic defects. The present contribution shows an in-depth study on the stages of formation and depletion of nanoparticulate CZTS. Employing a hot injection synthesis method, we give direct experimental evidence of the co-existence of cubic, tetragonal and defected CZTS structures and different by-products as a function of time and temperature. SEM, (HR)TEM, XRD, EDX, ICP-OES, Raman spectroscopy and UV-Vis-NIR spectroscopy have been used in order to better evaluate and interpret data for crystal structures and compositions. The obtained understanding on the formation of different phases suggests 250 °C as the most favourable synthesis temperature. Based on our study, general strategies can be developed for controlling the amount of formed phases, the by-products and the defects in kesterite and other similar multicomponent nanoparticles as well as in bulk systems.

 Received 4th April 2015,
Accepted 25th May 2015

DOI: 10.1039/c5ce00661a

www.rsc.org/crystengcomm

Introduction

One of the direct ways to convert sunlight into energy is by the use of photovoltaic technology. Sustainable energy solutions for the terawatt energy needs of the world require scalable and highly reproducible production of semiconductor materials using low temperature, low cost and eco-friendly industrial processes based on earth abundant materials.^{1,2} $\text{Cu}_2\text{ZnSnS}_4$ (CZTS) is considered to be a suitable absorber semiconductor with a tunable band gap, giving an opportunity to fully utilize the sunlight's spectrum.^{1,3,4} Additionally CZTS consists of earth abundant as well as non-toxic elements as compared to other semiconductors used in solar cells like CdSe/Te, PbS(e), CuInS_2 , Cu(In,Ga)(Se,S)_2 , CuInSe_2 etc.⁵ Presently, solar cells using CZTSSe have reached efficiencies as high as 12.7% leading to promising future perspectives.⁶

From a fundamental point of view, multicomponent particles are just one prominent example of materials with

complex composition, *i.e.* crystallinity and crystallographic phases have to be controlled together with size and shape of these particles. In fully crystalline form CZTS is found to exist in cubic, tetragonal (kesterite or stannite) and even hexagonal structures.^{7–10} In the cubic structure all metal atoms Cu, Zn and Sn take random positions in the unit cell (called face centred cubic (FCC)-disordered CZTS in our paper). In the tetragonal structure, Sn atoms take a fixed position while Cu and Zn atoms can still be ordered or disordered (called tetragonal CZTS in the succeeding part).⁷ For hexagonal CZTS, ordering of atoms is not studied so far. Ordering of the Zn and Cu atoms in the tetragonal structure defines kesterite or stannite forms of CZTS. Kesterite has alternating layers of cations CuSn, CuZn, CuSn and CuZn at $z = 0, 1/4, 1/2,$ and $3/4$ positions (c -axis of the tetragon), respectively. However, in stannite ZnSn layers alternate with CuCu layers at these positions. A detailed description of structural variations may be followed in the work of Paier *et al.*¹¹ It is worth noting that disordering in this sequence of metal atoms must not be confused with crystallographic defects (point, line, planar etc.). Crystallographic defects in these structures may give rise to hexagonal structures embedded within, often called wurtz-stannite.^{9,12} The complexity does not end here; all these structures may exist with by-products having similar characteristics. Further, their existence in amorphous form can never be neglected, especially in the case of nanoparticulate systems. A recent study¹³ further shows that there

^a Institute of Particle Technology, Friedrich-Alexander-Universität Erlangen-Nürnberg (FAU), Cauerstrasse 4, 91058 Erlangen, Germany.

E-mail: wolfgang.peukert@fau.de

^b Chair for Crystallography and Structural Physics, Friedrich-Alexander-Universität Erlangen-Nürnberg (FAU), Staudtstrasse 3, 91058 Erlangen, Germany

^c Center for Nanoanalysis and Electron Microscopy (CENEM), Friedrich-Alexander-Universität Erlangen-Nürnberg (FAU), Cauerstrasse 6, 91058 Erlangen, Germany

† Electronic supplementary information (ESI) available. See DOI: 10.1039/c5ce00661a

may also exist compositional inhomogeneity within a single nanoparticle. All these complexities pose tremendous challenges in the identification and/or differentiation of the main component from by-products.¹⁴

The synthesis of CZTS nanoparticles offers several advantages with respect to the bulk approach. In the first instance, it allows the production of inks that can be used in cost-efficient (at best) roll-to-roll printing processes.^{5,15} Moreover, the by-products or different structures often nucleate as single particles, distinct and well separated from the main product in the solution phase. Therefore, the by-products may be selectively separated after synthesis.^{1,16} This is however impossible to achieve in a bulk material where by-products, defected structures or disordered structures are incorporated in the produced layer in a non-separable way^{17,18} which also leads to ambiguous assignment of signals in characterisation techniques.

The formation of nanoparticles from solution requires a series of subsequent kinetic steps: reaction solutions must be mixed properly so that supersaturation as a thermodynamic driving force is built-up which in turn may trigger homogeneous and later heterogeneous nucleation followed by crystal growth and often also aggregation. The latter may be controlled by surface functionalization of the formed particles or by process parameters such as concentration or shear rates.^{19,20} Depending on their relative kinetics particle formation may be considered as either mixing or reaction controlled. Particle formation of “simple” systems²¹ can be modelled from a molecular perspective; modelling approaches of increasing complexity may even predict the dynamic evolution of particle size distributions and are the basis of any rigorous scale-up and process design.^{22,23} However, the underlying reaction mechanisms and reaction pathways are largely unknown for most systems. Therefore, fundamental investigations of the forming phases and by-products are considered as first important steps towards the understanding of formation mechanisms from which knowledge-based guidelines may be derived on how to control nanoparticle formation. For example, in the specific case of CZTS, it is not clear whether the formation of CZTS takes place since the early stages of reaction or if it is the result of inter-diffusion of secondary and ternary phases.

The formation and depletion of the CZTS phase are proposed to follow the overall reaction I,^{24,25} *i.e.*



Mostly, theoretical calculations based on thermodynamics and kinetics for such multiple compounds have been used to understand the equilibrium between phases during the formation of layers by thermal treatment on different substrates.^{24,25} The models predicting different structures,²⁶ phases⁵ and defects^{27,28} suggest that all these can co-exist in equilibrium and can significantly affect the efficiency of the final device.

Few experimental reports on the formation mechanism of wurtzite type CZTS nanoparticles have been presented.^{29,30} However, it must be noted that best efficiencies are reported for kesterite based solar cells.^{6,31} Recently, some reports on the mechanism and reaction pathways of formation of kesterite type CZTS nanoparticles have been published.^{32,33} Mostly, two different pathways are proposed, *i.e.* nucleation of Cu_{2-x}S followed by Sn and Zn diffusion and integration to form CZTS, and nucleation of Cu–Sn based compounds, *e.g.* Cu_2SnS_3 followed by Zn diffusion integration.^{32–34} However, these studies^{32,33} lack Raman analysis under the red laser and therefore ternary phases may not have been efficiently detected. Further, the XRD patterns presented in these publications^{32–34} only show cubic CZTS, and therefore, the proposed mechanism may not be directly applicable to kesterite (tetragonal) CZTS. Further, use of non-stoichiometric precursors³³ may lead to different reaction mechanisms in comparison to the synthesis with stoichiometric amounts of precursors. To the best of our knowledge, none of the studies on synthesis of CZTS nanoparticles address any temperature dependent formation of structural defects, their evaluation and their signature by comprehensive characterisation techniques. We further provide first evidence that CZTS is able to nucleate as a single phase and not just by diffusion of binaries and ternaries. Based on the kind of species that first nucleates, temperature dependence of reaction pathways is observed. In this regard we also provide insights into the stability of different by-products with respect to temperature including the formation of Raman active and inactive Cu_{2-x}S *etc.* Further, it must be noted that our synthesis approach involves no inert atmosphere, which makes it also the first mechanistic study in this regard.

The study employs the well-established, most widely used hot injection approach.⁴ It is carried out in continuation of our previous report³⁵ where, along with fully crystalline, non-defective CZTS nanoparticles, also particles with crystallographic defects were observed. The study presented leads to the development of general strategies for controlling the amount of different phases and defects in multicomponent nanoparticle systems synthesised by hot injection.

Synthesis of CZTS nanoparticles

Experimental details

Shortly, $\text{Zn}(\text{Ac})_2 \cdot 2\text{H}_2\text{O}$, CuCl_2 , and SnCl_2 were dissolved in stoichiometric molar ratios in oleylamine (OLA) and heated to the desired temperature. All the chemicals and the synthesis protocol for this study were essentially similar as reported earlier.³⁵ For this study 225 °C, 250 °C, 275 °C, 300 °C, and 330 °C were chosen as the injection as well as the growth temperatures. As soon as the desired temperature was reached, the homogeneous reaction mixture was left for a given time to ensure temperature homogeneity across the whole reaction volume. Then sulphur dissolved in oleylamine was injected. The reaction was allowed to run for 1 hour and then cooled to room temperature by using water on the outer wall of the

reactor. The temperature inside the reaction mixture was controlled and recorded carefully as shown in Fig. S1.† The details of the heating mantles and temperature controllers used are provided in the ESI.† To study the reaction kinetics at a fixed temperature, samples were taken out after 0 min, 5 min, 10 min, 20 min, 30 min and 60 min after the injection as shown in Fig. S2.† The syringe that was used to inject the sulphur was also used to take out a sample immediately after injection (designated as 0 min).

The obtained products were isolated by centrifugation (relative centrifugal force (RCF) ~2558, 30 min) and washed twice through centrifugation (RCF ~2558, 10 min) and dispersion cycles with a mixture of chloroform (20 mL) and methanol (50 mL). The product was then stored in suspension (25 g L⁻¹ in chloroform, stabilized by 20 wt.% OLA) and in powder (air dried) form for further characterisation using the following techniques.

(High resolution) transmission electron microscopy ((HR)TEM)

(High resolution) transmission electron microscopy ((HR)TEM) was performed using a Philips CM 300 UltraTWIN with a nominal point resolution of 0.17 nm at Scherzer defocus. The microscope was operated at 300 kV using a thermionic LaB6 filament. For TEM analysis the particles were drop casted on standard copper grids, supported with a continuous amorphous carbon film. The particle size distributions were measured by counting at least 150 particles at each temperature, following the procedure of Distaso *et al.*³⁶ Further, the TEM images were carefully analysed to identify the particles with crystallographic defects. A number percentage of such particles in relation to single crystalline particles was estimated within a sample.

Scanning electron microscopy (SEM)

Scanning electron microscopy (SEM) was performed to investigate the morphology and size of the samples. The instrument used was an ULTRA™ 55 (Carl Zeiss AG, Germany). Imaging was done under an accelerating voltage of 20 kV using a SE2 detector. The samples were prepared by drop casting the suspension on a silicon wafer and spreading the powdered sample on standard conductive carbon pads.

Energy-dispersive X-ray (EDX)

Energy-dispersive X-ray (EDX) was performed using EDX-ULTRA™ 55, Carl Zeiss AG, Germany, under an accelerating voltage of 20 kV. The samples for the analysis were prepared by pressing the powder into a pellet using a handheld press. Each sample was tested at a minimum of 10 different points in the sample.

Powder X-ray diffraction (PXRD)

Powder X-ray diffraction (PXRD) analysis was performed by classical *ex situ* PXRD in a Bragg–Brentano geometry using a Panalytical X'pert powder diffractometer with filtered Cu-K α

radiation and an X'Celerator solid-state stripe detector. Rietveld refinements were performed using the software MAUD (materials analysis using diffraction).

Raman spectroscopy

Raman spectroscopy was performed using confocal micro Raman (LabRam HR Evolution – HORIBA), with LabSpec 6 software, equipped with green and red excitation lasers of wavelengths 532.1 nm (Nd-YAG) and 632.8 nm (He-Ne), with average power on the sample surface less than 0.3 mW and 0.2 mW, respectively. The lasers were focused on powdered samples (pressed into a pellet) using a 50 \times objective with a nominal spot size of ~1.0 μ m.

Ultraviolet visible near infrared spectroscopy (UV-Vis-NIR)

Ultraviolet–visible spectroscopy (UV-Vis) was carried out using Lambda 35 (Perkin-Elmer – spectrometer). Quartz cuvettes (101-QS-Hellma) with an optical path length of 10 mm were used. Samples were analysed as suspension of particles in chloroform and stabilized by oleylamine.

Inductively coupled plasma–optical emission spectrometry (ICP-OES)

Inductively coupled plasma–optical emission spectrometry (ICP-OES) was performed using an ICP-OES Spectrometer Optima 8300 from Perkin Elmer. The organic rich supernatant was digested using microwaves (Multiwave 3000) from Anton Paar with 8 mL of HNO₃ and 1 mL of HCl. After the treatment a clear solution was obtained and used for ICP-OES analysis upon appropriate dilution.

For such a sensitive and complicated material system, all the experiments and related characterizations have been repeated at least four times to ascertain reproducibility.

Results and discussion

Characterization of as-synthesised CZTS nanoparticles

(High resolution) transmission and scanning electron microscopy. Fig. 1(a–d) show the bright-field TEM images of as-synthesised products. The particles at different temperatures appear to have a range of different shapes and sizes. One of the unique features observed in all the samples was the co-existence of single crystalline and defected particles, showing twinning (Fig. 1(i–ii) – an example from 300 °C). The lattice spacing of 3.1 Å was found for single crystalline particles which corresponds to either the (112) plane of tetragonal CZTS or the (111) plane of cubic CZTS, yielding the most intense reflections in the XRD pattern.

The equivalent diameter (x) of a sphere with the same projected area as the particles was calculated from TEM images. The cumulative distributions obtained by counting a minimum of ~200 particles are shown in Fig. 2 (corresponding density distributions, see Fig. S6†). The number-based median size decreases with increasing reaction temperature between 15.2 nm at 225 °C and 6.5 nm at 300 °C. The change

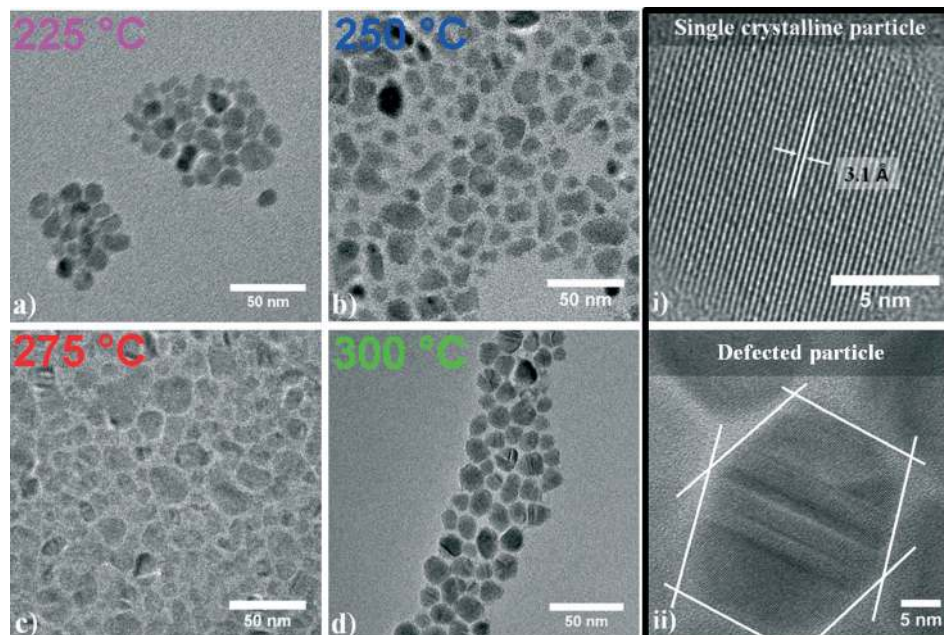


Fig. 1 (a–d) Bright-field TEM images of as-synthesised nanoparticles at different temperatures showing size and shape. An example of HRTEM images from the 300 °C sample i) showing a single crystalline spherical particle and ii) a particle with a twinned structure.

in the mean number-based diameter ($x_{50,0}$) from 225 °C to 275 °C is about 18%. However, there is a jump in size reduction from 275 °C to 300 °C, and the $x_{50,0}$ reduces by about 48%; in total from 225 °C to 300 °C, a reduction of about 57% is observed.

Fig. 3 shows a detailed HRTEM analysis of a defected particle including Fast Fourier transformation (FFT) of the image (inset) and a magnified view of a selected region. FFT analysis shows three sets of lattice planes with lattice spacings of 3.1 Å, 2.7 Å and 1.9 Å. In the magnified view (Fig. 3b) face centred cubic (FCC) stacking of the atoms can be seen with a hexagonal sequence appearing as a result of stacking faults. Therefore, these lattice spacings can be associated

with (111), (200) and (220) planes of a FCC structure, respectively. Additionally, it is evident that the stacking faults have caused twinning in the crystal structure. In FCC structures twinning is known to occur along $\{111\}$ planes which is also evident in FFT analysis ((111) twin plane marked with asterisks). These twinned particles are referred to as defected particles in this paper.

The number percentage of such defected particles is shown in Fig. 4. For this purpose a minimum of 150 particles were analysed. It can be seen that the relative amount of defective particles is small and almost constant at lower temperatures whereas a sharp increase occurs at 300 °C. Simultaneously, particle size decreases more strongly above 275 °C (Fig. 2). It must be noted that such defected particles can be seen in many different kinds of nanoparticles synthesised by hot injection.^{37–39} For example, these defects can be observed in $\text{Cu}_2\text{ZnSnSe}_4$ ³⁹ and CuInS_2 ⁴⁰ nanoparticles, and often appear as contrast difference within a single particle. However, any relation between these defected particles and the synthesis parameters and their signatures in different characterisation techniques has not been established so far in the literature.

Interestingly, the reaction product at 330 °C turned out to be very different in shape and size as compared to other reaction products. Fig. 5(a–d) shows representative TEM and SEM images of the as-synthesised product at 330 °C, respectively. The sample mainly consists of hexagonal and well faceted structures ($\sim 1 \mu\text{m}$) clustered in a matrix of smaller less faceted (spheroidal) particles ($\sim 50 \text{ nm}$).

Energy-dispersive X-ray (EDX) and inductively coupled plasma–optical emission spectrometry (ICP-OES). EDX analysis was carried out to determine the elemental composition of the as-synthesised products at different temperatures.

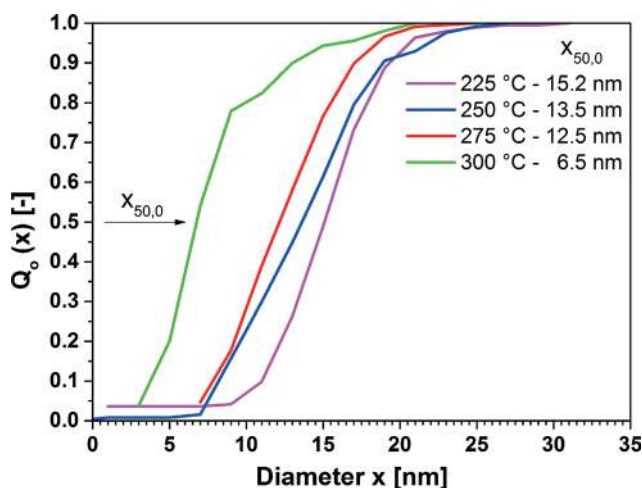


Fig. 2 Cumulative number distributions as obtained by counting a minimum of ~ 200 particles synthesised at different temperatures showing a decrease in mean size with increasing reaction temperature.

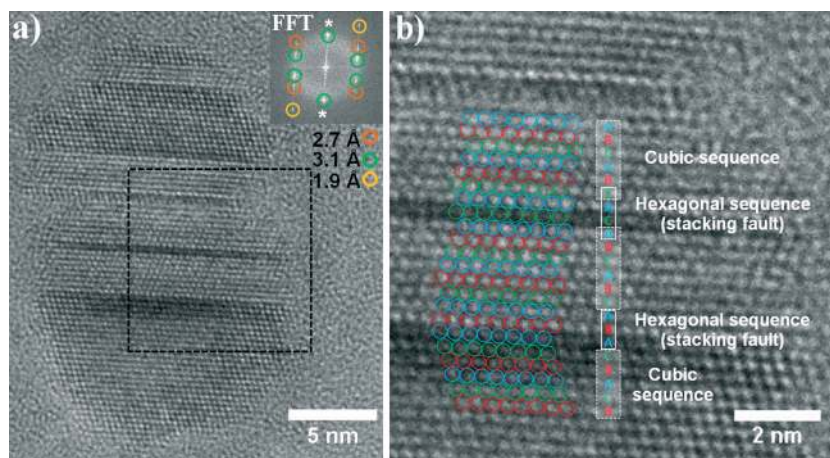


Fig. 3 HRTEM analysis of a defected particle: a) view of several twin planes with FFT analysis (inset), b) magnified view of the selected region showing FCC stacking of the atoms within the particle and hexagonal stacking faults.

Fig. 6a shows the ratios of various elements with respect to copper and the sum of the metal content in the sample. It can be observed that the products at lower temperatures, namely at 225 °C and 250 °C, are similar in stoichiometry and very close to the ideal ratios in CZTS with a minor deficiency in Cu and Zn. However, above 250 °C Zn, Sn and S contents of the product drop until 330 °C where almost no Zn and Sn are present in the product.

It can be seen in Fig. 6a that the change in the Zn content is most pronounced, followed by the Sn and S contents. However, it is worth noting that Zn and S contents decrease gradually from 225 °C to 330 °C in contrast to Sn, which is mainly constant until 275 °C and drops rapidly after 300 °C.

Additionally, the micron sized hexagonal structures formed at 330 °C (as shown in Fig. 6b) were analysed using EDX. The analysis showed that these hexagons only consisted

of S and Cu whereas Zn and Sn were not detected at all. Fig. 6c shows that the S:Cu ratio in four of such hexagonal structures varies between 0.54 and 0.6, which corresponds to different Cu_{2-x}S phases ($x = 0, 0.03, 0.2, 1$) that co-exist in the sample.^{41–43}

Further, the supernatant obtained after the first centrifugation was analysed using ICP-OES (Table S1†) for 250 °C and 300 °C. The supernatant for the 300 °C reaction was found to be highly rich in Zn, Sn and S as compared to the reaction at 250 °C. The elemental and TEM analyses do not give any information about the existence of any particular

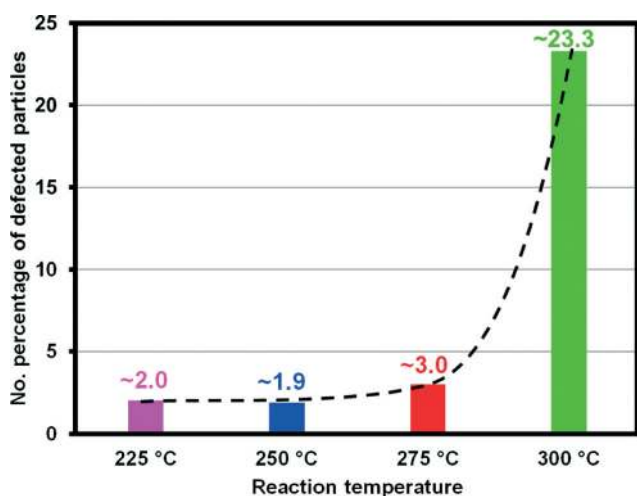


Fig. 4 Number percentage of particles (out of approx. 150 particles) having crystallographic defects showing a steep increase in the number of defected particles for temperatures above 275 °C (data as obtained from HRTEM image analysis).

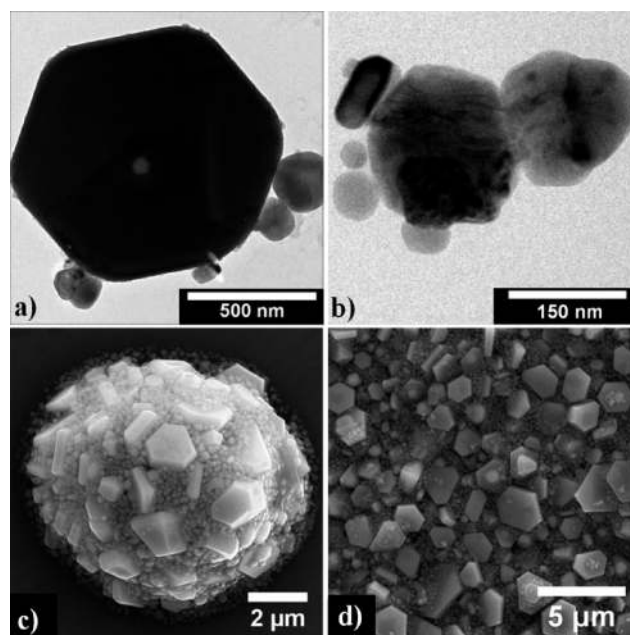


Fig. 5 TEM and SEM images of a product synthesised at 330 °C: a) hexagonal particles (as large as 1 μm) with b) less faceted or spheroidal smaller particles of around 50 nm; c, d) SEM images showing micron sized hexagonal particles embedded in agglomerates together with smaller ~50 nm spheroidal particles.

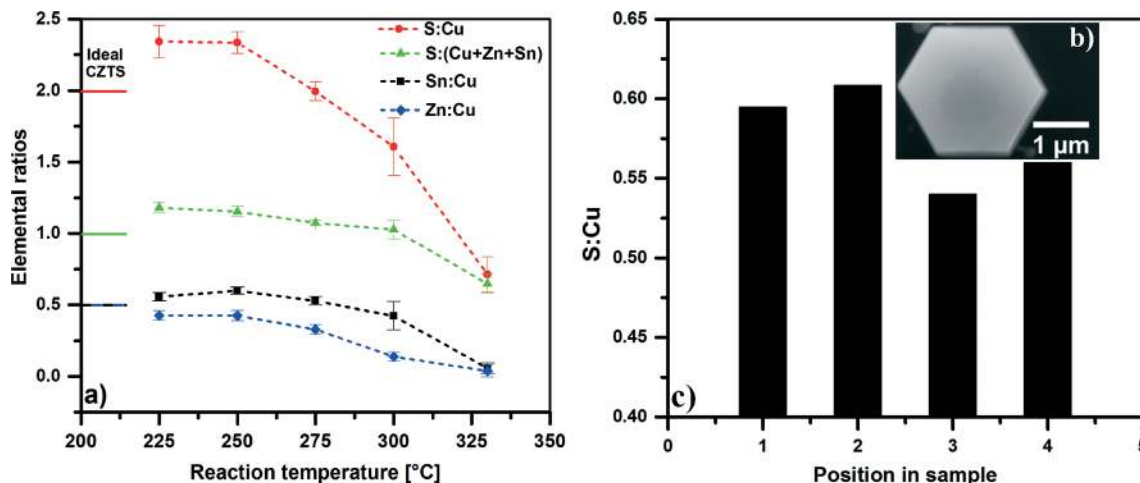


Fig. 6 EDX analysis a) of products synthesised at different temperatures, showing a continuous decrease in the Zn, Sn and S contents with increasing injection temperature, and b) of micron sized hexagons synthesised at 330 °C, and c) the variation in composition for four of the analysed hexagons in the sample.

phase. However, both methods allow us to draw the following two conclusions:

- The solid product (being always Zn poor) is more prone to have Cu-rich phases as compared to Zn-rich, especially at high temperatures.
- The increasing number of defected particles is mainly a result of successive Zn and Sn deficiencies.

In addition to these two conclusions the presence of different phases was studied by the following XRD and Raman analyses. Then a correlation among all the techniques is established to explain the reaction mechanism.

X-ray diffraction (XRD). The diffraction patterns of the samples synthesized at 225 °C, 250 °C and 275 °C were found to be very similar as shown in Fig. 7. A recent study carried out on a CZTS nanoparticulate sample synthesized at a temperature as low as 225 °C showed that the particles crystallize in a disordered FCC phase.⁴⁴ In this study, a phase transition from the disordered FCC phase to the tetragonal phase was observed by *in situ* XRD during sample annealing. The identification of the tetragonal structure was associated with the appearance of 002 (~16.3°), 101 (~18.2°), and 110 (~23.1°) reflections in addition to cubic reflections (as marked in

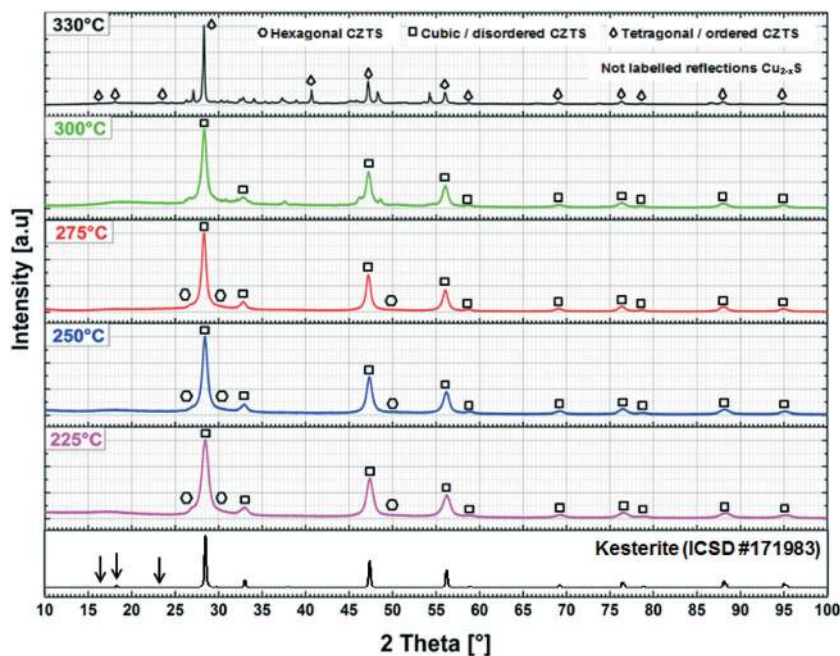


Fig. 7 XRD patterns of the as-synthesised products at different temperatures.

Fig. 7). Therefore, an ordered arrangement of the cations in the unit cell is not observed for temperatures below 330 °C. Similar diffraction patterns have been assigned to a cubic CZTS structure with a disordered cation arrangement in the unit cell.^{7,45}

The diffractograms of these three samples have clearly visible shoulders on the side of the cubic 111 as the most intense reflection. Rietveld refinements (example, Fig. S3† for 250 °C) have shown that the measurements can be best modelled by a cubic $F\bar{4}3m$ CZTS phase and a hexagonal $P63mc$ wurtzite CZTS phase (Fig. S4†). Because of the seemingly anisotropic peak widths of the wurtzite phase we used a microstructure model that follows ref. 46. The results of the microstructure refinement show that the crystallites of the wurtzite phase are disc-shaped with elongation in the AB -plane. Consequently, the 002 reflection ($\sim 28^\circ$) in the refined diffractograms almost completely vanishes (Fig. S3†). Together with the HRTEM images this indicates that the wurtzite phase exists as stacking faults in the cubic CZTS. The as-obtained lattice parameters of the two phases are presented in Table S1.† Further analysis shows that in the 250 °C sample the intensity contribution of this hexagonal phase is the lowest among the three samples.

The 300 °C and 330 °C samples were different from the others. In these samples reflections from secondary phases in addition to the CZTS have been observed clearly. The pattern of the 300 °C sample can be best modelled using the cubic CZTS and a monoclinic $P2_1/n$ “Djurleite” $\text{Cu}_{1.94}\text{S}$ phase.⁴² Due to a relatively high number of intense reflections from Djurleite, the scattering contributions from the wurtzite CZTS structure are difficult to identify in this pattern and are therefore not introduced in the fitting model. Furthermore, the mean particle size reduced by 57% from 15.2 nm (225 °C) to 6.5 nm (300 °C) while simultaneously the internal stresses increased due to the existence of more defects leading to broadening of the XRD reflections, and therefore wurtzite reflections were difficult to observe. It is worth noting that smaller particle sizes might also contribute to peak broadening.

Even more reflections from secondary phases appear in the measurement of the 330 °C sample. In this case all secondary signals can be well explained by copper sulphides with different stoichiometries and structures. Most probably, there is a mixture of the already mentioned Djurleite ($\text{Cu}_{1.94}\text{S}$) and the chalcocite Cu_2S in monoclinic $P2_1/c$ and hexagonal $P6_3/mmc$ structures,^{42,47} respectively. The reason for this uncertainty in phase identification is that these copper sulphide structures can coexist in an inter-grown state and may easily be converted into each other.⁴⁸ With this interpretation of the measurements, the hexagonal crystallites seen in the SEM images can be identified as monoclinic Djurleite that is morphologically influenced by pseudo-hexagonal twinning.⁴⁸ These data are also in agreement with the EDX results reported in Fig. 6c.

Another important feature of the 330 °C sample is that it is the only sample in the series that clearly shows a

tetragonal structure of the CZTS, meaning a well ordered arrangement of Sn atoms in the unit cell. However, whether this is a kesterite or a stannite type structure cannot be distinguished using the applied method because of the missing scattering contrast between Cu and Zn atoms. There is no signal from the wurtzite type defects in this sample which is probably correlated with the appearance of Cu_{2-x}S phases. Additionally, the width of the reflections of the CZTS in this sample is significantly smaller than in the other samples hinting at an increased size of the CZTS crystallites as observed in TEM and SEM as well.

It is worth noting that cubic and orthorhombic phases like ZnS, Cu_2SnS_3 and Cu_3SnS_4 (collectively CTS), respectively, cannot be easily distinguished using XRD.⁴⁹ We modelled XRD patterns with several combinations of such phases. However, the best fit resulted only in the combination of the phases (cubic CZTS, wurtzite CZTS and Cu_{2-x}S) mentioned above for each reaction product. Additionally, the elemental analysis shows that the product at each reaction temperature is Zn-poor. On the basis of thermodynamics, the formation enthalpy (ΔH_f) of CZTS is 150 kJ mol^{-1} lower than that of ZnS.³⁵ Therefore, in a Zn-poor material system the probability of formation of ZnS is smaller as compared to CZTS or CTS. This is especially true for the product at 300 °C. Therefore, it can be stated that either other phases were not present in the respective products or these were below the detection limit of the device.

There is a rapid decrease in the Sn content of the product after 300 °C. This loss results in the final conversion of defected particles into the Cu_{2-x}S phase (because of excessive Zn and Sn loss), and therefore no defected particles were seen at 330 °C. To support and strengthen the above arguments and to further confirm the presence or absence of different phases especially in the amorphous form, Raman analysis was performed.

Raman spectroscopy. Raman spectroscopy has been extensively used as a key method for the identification of CZTS in comparison to various by-products not identifiable otherwise in such a multicomponent material system.⁴⁹ Fig. 8 shows a set of Raman spectra for each synthesised product at different temperatures using green and red lasers. All the significant Raman shifts have been marked.

It can be seen that for the synthesis carried out at 225 °C and 250 °C (Fig. 8a and b), the most intense characteristic Raman shift for CZTS is seen at 337 cm^{-1} (mode A). The second most intense peak is rather seen as a broad shoulder at 295 cm^{-1} . It must be noted that for nanoparticles (size effect), capped with surfactants (oleylamine), having variation in the sulphur content and stresses and strains in the material, Raman signals are known to shift and are generally broad.³⁵ Therefore, the Raman shift at 295 cm^{-1} can either be attributed to mode A – kesterite (285 cm^{-1} – 290 cm^{-1}) or mode B – stannite (292 cm^{-1}).³⁵ However, the XRD analysis showed that our product at low temperature consists mainly of FCC disordered CZTS together with a small amount of defected (wurtzite type) CZTS, whereas no tetragonal structure was observed. The other very weak humps in the 225 °C reaction

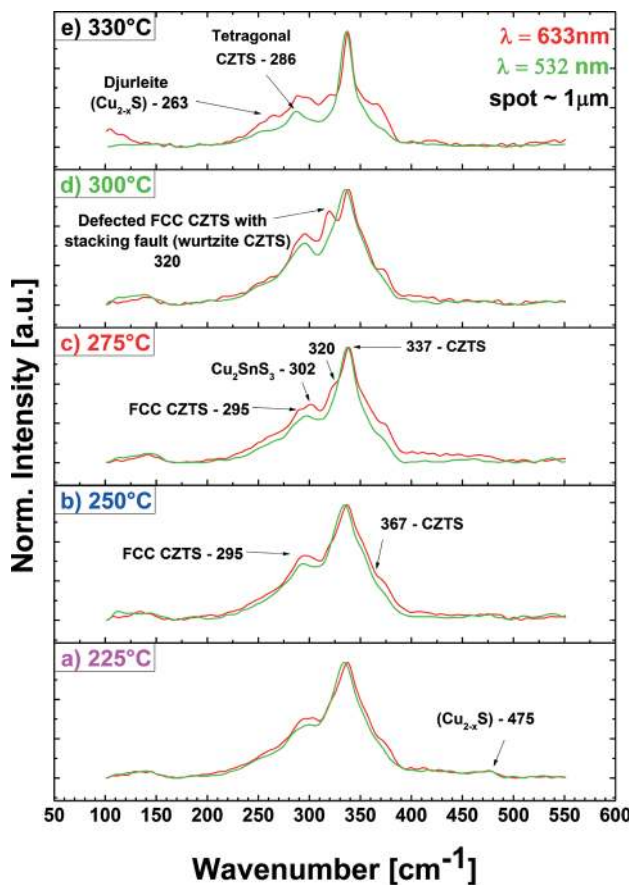


Fig. 8 Raman spectra (using green and red lasers) of as-synthesised reaction products obtained at different temperatures showing the evolution of different phases as a function of temperature.

product at 475 cm^{-1} and 302 cm^{-1} may be attributed to the existence of Cu_{x-2}S ³⁵ and Cu_2SnS_3 ⁵⁰, respectively. It is worth noting that for both green and red lasers the spectra look very similar with no clear evidence of any by-products.

For the reaction product at $275\text{ }^\circ\text{C}$, an additional Raman shift at 320 cm^{-1} can be observed (Fig. 8c). The origin of this shift at 320 cm^{-1} is rather unclear. Various groups have attributed this shift to the existence of SnS_2 ,⁴⁹ Cu_3SnS_4 ^{30,50,51} or even CZTS.^{52,53}

The increase in the number of defected particles (Fig. 4) with increasing injection temperature and corresponding increase in intensity of the peak at 320 cm^{-1} suggests that this peak is due to defected particles. The existence of these defected structures is often reported in $\text{I}_2\text{-II-IV-VI}_4$ semiconductors.^{9,12,26,28,54} In all these reports such a structure is either calculated or fitted to XRD patterns of bulk synthesised or annealed CZTS and therefore not easily identifiable. However, in our case imaging of separated nanoparticles together with XRD analysis gave a direct evidence of the existence of wurtzite type defects in disordered cubic CZTS. Interestingly, this Raman shift at 320 cm^{-1} , the shoulder to the left of the most intense 111 XRD reflection, and defected particles in TEM can also be observed in CZTS nanoparticles synthesised by a different synthesis protocol.^{13,55} These reports^{13,55}

confirm that there exist elemental inhomogeneity within their particles. Therefore, it can be postulated that the bulk deficiency of Zn and Sn that we observe in our particles is probably the cause of structural inhomogeneity (defects). Further, it must be noted that this Raman shift is different from the shift of wurtzite type CZTS ($\sim 333\text{ cm}^{-1}$ to $\sim 336\text{ cm}^{-1}$).^{29,55} All these arguments taken together give sufficient reasons to assign this shift to defected regions in FCC CZTS. Due to the stacking faults (elemental inhomogeneity) the surrounding of the sulphur atom is expected to be different, and therefore, a characteristic Raman shift should be observed.

The particles synthesised at $330\text{ }^\circ\text{C}$ show all the above mentioned Raman shifts. However, the shift at 295 cm^{-1} has moved to 286 cm^{-1} which is now closer to mode A – kesterite. This is in accordance with XRD analysis and confirms ordering of cations from the cubic to the tetragonal phase. Moreover, the shift at 320 cm^{-1} only shows up as a weak shoulder in contrast to the reaction product at $300\text{ }^\circ\text{C}$. This is in good agreement with data from TEM, XRD and EDX (loss of Zn and Sn) which show the co-existence of three processes: disappearance of defected particles, formation of Djurleite ($\text{Cu}_{1.94}\text{S}$), and transition from cubic to tetragonal CZTS. Since Djurleite is weakly Raman active only a weak shoulder at 263 cm^{-1} can be observed in this spectra.⁵⁶

Ultraviolet-visible-near infrared (UV-Vis-NIR) spectroscopy. Fig. 9 shows a set of extinction spectra normalized to the maximum intensity of all the products synthesised at different temperatures. It can be seen that the extinction decreases with increasing injection temperature. All the spectra look very similar until the synthesis at $300\text{ }^\circ\text{C}$ and are similar to reported spectra for CZTS.³⁵ For the synthesis carried out at $330\text{ }^\circ\text{C}$ a broad band is seen ranging from 450 nm to 1000 nm which can be attributed to Cu_{x-2}S .⁴³

The data clearly show that low temperatures ($T \leq 300\text{ }^\circ\text{C}$) favour the formation of CZTS in an FCC disordered phase, whereas at higher temperature ($T \geq 300\text{ }^\circ\text{C}$) the final product consists of tetragonal CZTS as well as secondary phases.

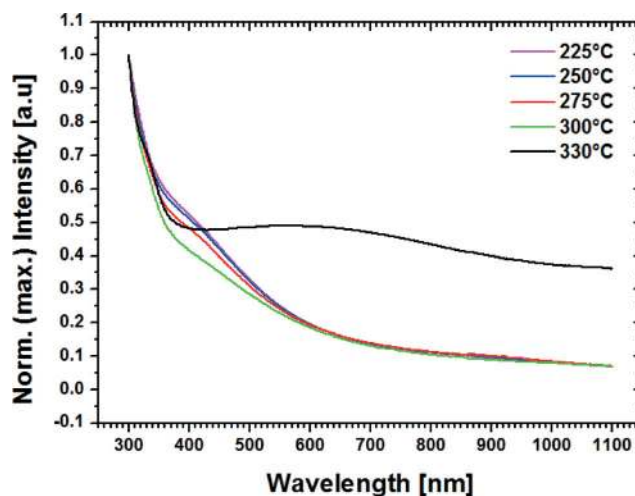


Fig. 9 UV-vis-NIR spectra of the suspensions of different products obtained at different reaction temperatures.

Therefore, by control of the temperature of injection the yield of the CZTS phase can be maximized. However, a question arises at this point of the discussion whether the secondary phases formed at higher temperature are the consequence of a decomposition of the product during the reaction at high temperature, or are formed by a co-nucleation and growth process.

Another aspect is related to the more general question about the mechanism of formation of CZTS itself; *i.e.* does it form through a nucleation and growth process of the four component phase (Cu–Zn–Sn–S), or through the interdiffusion of binary and secondary phases? In order to answer these questions, a kinetic study was carried out at 250 °C and 330 °C in order to draw conclusions about the formation mechanism.

Reaction kinetics at 330 °C and 250 °C. Fig. 10a shows elemental analysis of the samples taken out after different time intervals for 330 °C reaction. Since a continuous change in the stoichiometry of the product is seen in EDX, a continuous change in the phases is also expected with time in Raman analysis (Fig. 11a). It is interesting to see that immediately after injection a co-nucleation of SnS (190 cm^{-1} and 221 cm^{-1}), Cu_2SnS_3 (302 cm^{-1} and 355 cm^{-1}), defected FCC CZTS (318 cm^{-1}), CZTS (331 cm^{-1}) and Cu_{2-x}S (472 cm^{-1}) can be observed.⁴⁹ As the time of reaction increases the SnS and Cu_{2-x}S peaks disappear successively and defected CZTS peaks become stronger until 10 min. The Sn, Zn and S contents of the product are decreasing continuously (Fig. 10a). Therefore, dissolution of the binaries into the solution phase as well as removal of Zn from CZTS to form more of defected CZTS is suggested. After 10 min, only the Raman shifts for CZTS can be observed and the peak for defected CZTS completely disappears. As EDX show very low Sn and Zn contents, this indicates conversion of defected CZTS into Cu_{2-x}S . However, this Cu_{2-x}S does not give strong Raman signals and is only well

identified and characterised for the 60 min sample by XRD and SEM (Fig. 6 and 7) where along with this Cu_{2-x}S a CZTS tetragonal structure is also observed.

The phase distributions observed at different temperatures for a fixed time fit very well to the observed phase distributions in dependence of time at fixed temperatures of 250 and 330 °C, respectively. HRTEM and SEM images of these samples are provided in the ESI† (Fig. S4).

For the reaction at 250 °C, it can be seen (Fig. 10b) that after about 10 min there is no more change in the stoichiometry of the samples. This leads to the assumption that steady state conditions between the solid phases formed and the liquid phase prevail. Raman analysis (Fig. 11b) for these sample shows that immediately after injection (0 min) a broad Raman peak can be observed between 200 cm^{-1} and 400 cm^{-1} which indicates a co-nucleation of by-products with CZTS. The possible products can be Cu_2SnS_3 and ZnS because their Raman signals are located in this region, but are not visible. Additionally, there exists a very distinct peak for Cu_{2-x}S at 475 cm^{-1} .

As the time increases the Cu_{2-x}S peak disappears and the weaker Raman shift (295 cm^{-1}) for FCC disordered CZTS becomes visible. This indicates conversion of reactants (increasing Sn and S contents as seen in EDX – Fig. 10b) and/or by-products into the favoured CZTS formation. After about 10 min there is no remarkable change in the Raman spectra which is in agreement with EDX analysis and confirms that the reaction is almost complete after 10 min, *i.e.* equilibrium is almost reached. HRTEM and SEM images of these samples are provided in the ESI† (Fig. S5).

Proposed mechanism

In the light of the above results, mechanisms for formation and depletion of CZTS phases are proposed. The co-existence

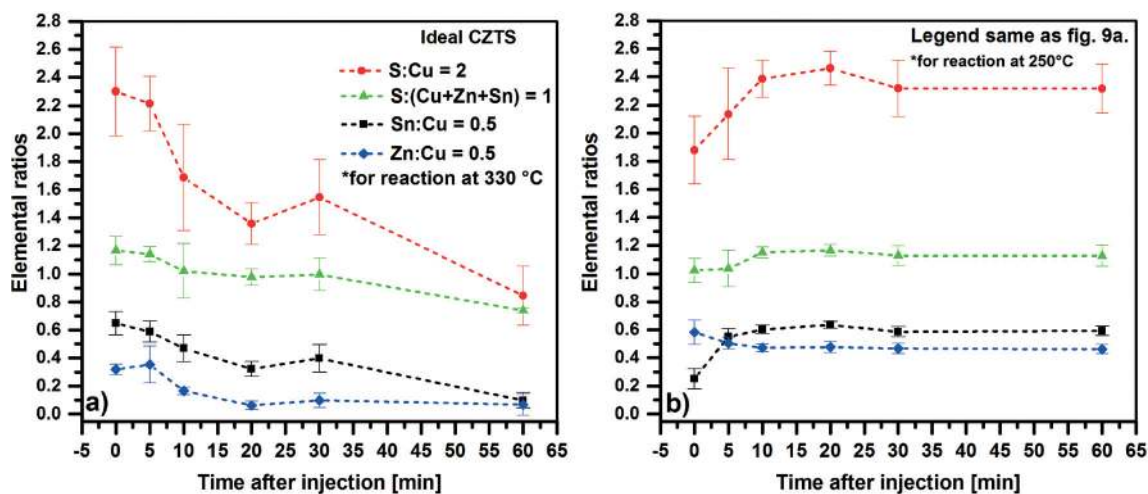


Fig. 10 Elemental analysis of samples taken out at different time intervals after injection: a) reaction carried out at 330 °C using EDX spectroscopy, showing a continuous decrease of zinc, tin and sulphur contents of the product with increasing time, b) reaction carried out at 250 °C using EDX spectroscopy, showing formation of steady state composition after ~10 minutes.

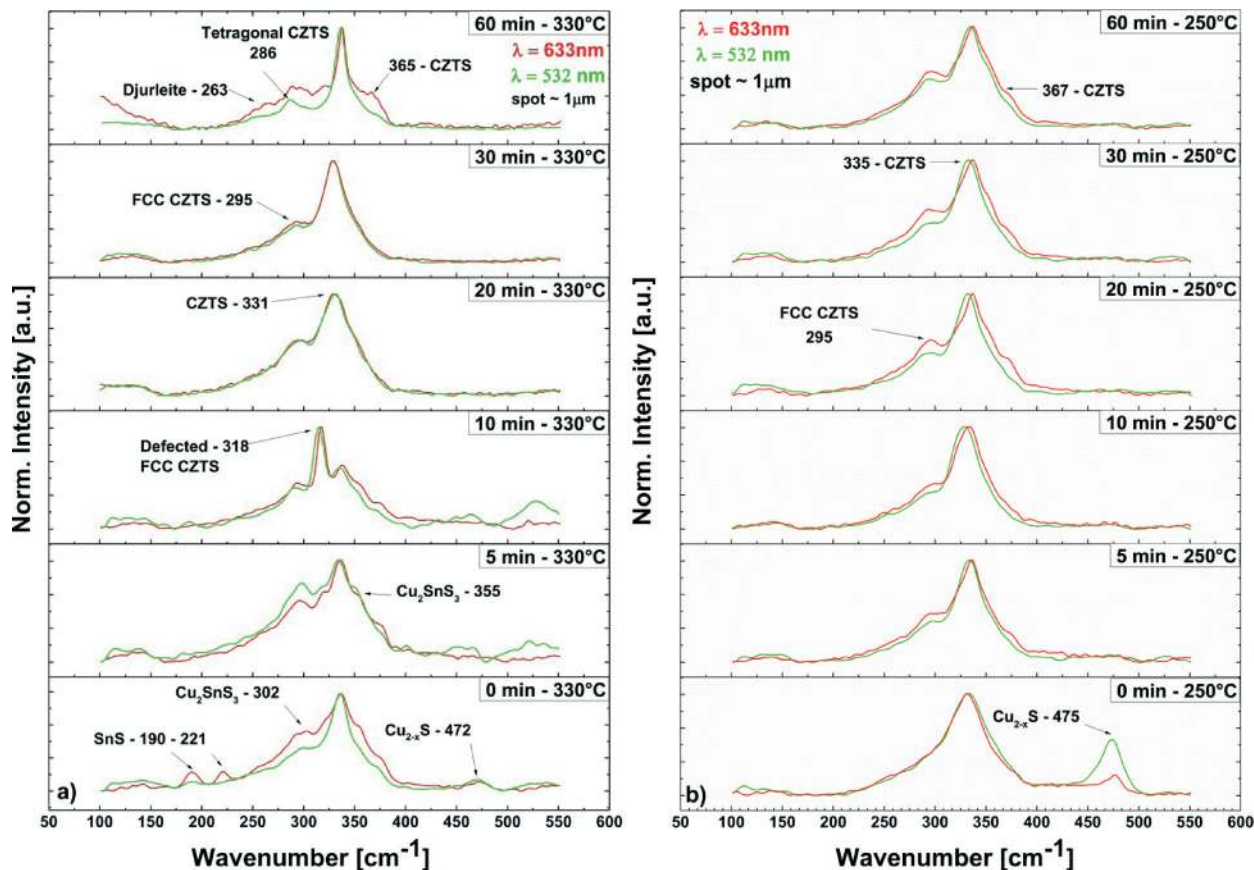


Fig. 11 Raman analysis of samples taken out of reactions carried out at a) 330 °C and b) 250 °C at different time intervals showing formation of different phases with increasing reaction time.

of different phases and structures at different temperatures and their inter-conversion is summarised in Table 1. At each temperature the product can be considered as consisting of several fractions, *i.e.* FCC (disordered) CZTS, defected FCC CZTS particles and by-products.











It can be seen that disordered FCC CZTS nucleates at all temperatures directly (at least on the time scale of our study). As the synthesis temperature is increased from 225 °C to 250 °C, the percentage of FCC-disordered CZTS nanoparticles increases (Fig. 4), whereas the small amounts of Cu_{2-x}S and Cu_2SnS_3 seen at 225 °C (Fig. 8) are no longer observed in the 250 °C product. This suggests that these binaries and ternaries have got enough energy to diffuse into the defected particles and form FCC disordered particles. Such a mechanism is also proposed for the formation of wurtzite CZTS.³⁰

However, when the reaction is carried out above 250 °C, the number percentage of defected CZTS nanoparticles increases (Fig. 4). The Zn deficiency (Fig. 6) goes in parallel with the increase in the number of defected CZTS nanoparticles, resulting in formation of Cu_2SnS_3 as observed by Raman spectroscopy analysis (Fig. 8). Corresponding to the formation of these Cu-rich phases, formation of ZnS is also expected. However, owing to its higher solubility,¹ it remains in the mother liquor and therefore, the corresponding Zn and S amounts are found in the supernatant (Table S2[†]). It

must be noted that 250 °C can only be considered as local equilibrium for favourable CZTS formation under the given conditions. The reaction pathway may be very sensitive to first nucleated species at a given temperature. The size, solubility, melting point and thus supersaturation and their mutual interactions must play a vital role. As an example Cu_{2-x}S can be observed below and above 250 °C. However it must be noted that below 250 °C only Raman active Cu_{2-x}S is seen, and above 250 °C a different mixed phase (Djurleite and chalcocite) Cu_{2-x}S is observed. It can be nicely seen in the kinetics at 330 °C, how one kind of Cu_{2-x}S changes into another type as a function of time and temperature. Stability and metastability of different Cu_{2-x}S phases on the basis of stoichiometry, time and temperature are further supported in the literature.^{42,43,48} Therefore, we conclude that at 250 °C thermodynamic and kinetic conditions were most favourable for formation of FCC CZTS with respect to other by-products or defected CZTS.

With increasing temperature ($T \geq 300$ °C) the formation of the defected structure continues at the cost of FCC-disordered CZTS (Fig. 4 and 8). However, it must be noted that at the same time the cations in FCC disordered CZTS rearrange and the tetragonal CZTS phase is observed at 330 °C. Additionally, a continuous removal of Zn and Sn from Cu_2SnS_3 results in the formation of Djurleite ($\text{C}_{1.94}\text{S}$).

Table 1 Proposed mechanism for formation of defects and co-existence of various CZTS phases

	Fraction I	Fraction II
225°C	 FCC (disordered) CZTS(s)	 FCC disordered CZTS with wurtzite CZTS as stacking faults + Cu_{2-x}S + CTS
	Mean size ~ 15.8 nm	
250°C	 FCC (disordered) CZTS(s)	 FCC disordered CZTS with wurtzite CZTS as stacking faults
	Mean size ~ 14.7 nm	
275°C	 FCC (disordered) CZTS(s)	 Highly defected FCC CZTS(s) + $\text{Cu}_2\text{SnS}_3(\text{s})$ + $\text{ZnS}(\text{l})$ + $\text{S}(\text{l})$
	Mean size ~ 13.4 nm	
300°C	 FCC (disordered) CZTS(s)	 Highly defected (wurtzite) CZTS(s) + $\text{Cu}_2\text{SnS}_3(\text{s})$ + $\text{Cu}_{2-x}\text{S}(\text{s})$ + $\text{ZnS}(\text{l})$ + $\text{SnS}_2(\text{l})$ + $\text{S}(\text{l})$
	Mean size ~ 8.8 nm	
330°C	 Spherical – Tetragonal CZTS(s)	 Hexagonal $\text{Cu}_{2-x}\text{S}(\text{s})$ and remains of other phases
	Mean size ~ 50 nm	Mean size ~ 1 μm

Therefore, it can be concluded that CZTS nucleates at all temperatures whereas temperatures above 250 °C favour the formation of secondary phases or defected particles. The inter-conversion and co-nucleation of different phases can be controlled by injection temperature and reaction time.

Considering the above discussed mechanism, strategies can be suggested to obtain stoichiometric or Cu-poor products by increasing or decreasing the amount of respective elements in the precursors. However, the excess of one element may trigger formation of other by-products enriched in that element and therefore alter the reaction pathway.

Conclusion

In the present work, we have revealed the various stages related to formation, co-existence and depletion of various CZTS phases and by-products as a function of the injection temperature and reaction time. The combination of complementary characterisation techniques has led to the comprehensive identification of different phases. As a result the study showed for the first time that CZTS nucleates at all temperature and its relative amount can be controlled by controlling injection and growth temperature. At temperatures as low as 225 °C and 250 °C the formation of FCC disordered CZTS was observed whereas at higher temperatures (>300 °C) tetragonal CZTS was formed.

It was found that the as-synthesized samples comprise particles with a wurtzite structure within the FCC disordered CZTS. The number percentage of such defected particles has been correlated with the synthesis temperature and found to increase when the injection temperature increases with a maximum at 300 °C. These defected particles present a unique signature in Raman spectroscopy and XRD. By increasing the injection temperature, progressively Zn-, Sn- and S-deficient particles together with by-products were obtained. At 330 °C Raman inactive Cu_{2-x}S was identified. An injection temperature of 250 °C was found to be the optimum for the formation of FCC disordered CZTS particles with a minimum of defects and by-products.

The formation of defected particles seems to be inherent to the hot injection method of synthesis and can be observed in almost all kinds of CZTS nanoparticles made by this method (mostly irrespective of synthesis protocol).^{1,55} The formation of defected structures is not only limited to CZTS but is also observed for CZTSe, CIS, and CIGS nanoparticles synthesised by similar hot injection methods.¹⁶ The results presented in this study related to defects may be generalized for I-III-VI₂ and I₂-II-IV-VI₂ type nanoparticles synthesised by hot injection.⁴ Moreover, understanding of the formation mechanism can help to formulate synthesis and annealing strategies to maximise the formation of kesterite type CZTS.

Acknowledgements

The authors acknowledge BAYER Technology Services for financial support. This work was supported by the Deutsche

Forschungsgemeinschaft through the Cluster of Excellence 'Engineering of Advanced Material' initiative at the 'Friedrich Alexander University of Erlangen-Nuremberg'. The authors also thank Ms. Paula Hoppe for her help in ICP-OES analysis.

References

- 1 H. Zhou, W.-C. Hsu, H.-S. Duan, B. Bob, W. Yang, T.-B. Song, C.-J. Hsu and Y. Yang, *Energy Environ. Sci.*, 2013, **6**, 2822–2838.
- 2 M. V. Kovalenko, L. Manna, A. Cabot, Z. Hens, D. V. Talapin, C. R. Kagan, V. I. Klimov, A. L. Rogach, P. Reiss, D. J. Milliron, P. Guyot-Sionnest, G. Konstantatos, W. J. Parak, T. Hyeon, B. A. Korgel, C. B. Murray and W. Heiss, *ACS Nano*, 2015, **9**, 1012–1057.
- 3 D. Aldakov, A. Lefrançois and P. Reiss, *J. Mater. Chem. C*, 2013, **1**, 3756–3776.
- 4 U. Ghorpade, M. Suryawanshi, S. W. Shin, K. Gurav, P. Patil, S. Pawar, C. W. Hong, J. H. Kim and S. Kolekar, *Chem. Commun.*, 2014, **50**, 11258–11273.
- 5 H. Azimi, Y. Hou and C. J. Brabec, *Energy Environ. Sci.*, 2014, **7**, 1829–1849.
- 6 J. Kim, H. Hiroi, T. K. Todorov, O. Gunawan, M. Kuwahara, T. Gokmen, D. Nair, M. Hopstaken, B. Shin, Y. S. Lee, W. Wang, H. Sugimoto and D. B. Mitzi, *Adv. Mater.*, 2014, **26**, 7427–7431.
- 7 S. Schorr and G. Gonzalez-Aviles, *Phys. Status Solidi A*, 2009, **206**, 1054–1058.
- 8 S. Siebentritt and S. Schorr, *Prog. Photovolt: Res. Appl.*, 2012, **20**, 512–519.
- 9 S. Chen, A. Walsh, Y. Luo, J.-H. Yang, X. G. Gong and S.-H. Wei, *Phys. Rev. B: Condens. Matter Mater. Phys.*, 2010, **82**, 195203.
- 10 A. Singh, S. Singh, S. Levchenko, T. Unold, F. Laffir and K. M. Ryan, *Angew. Chem., Int. Ed.*, 2013, **52**, 9120–9124.
- 11 J. Paier, R. Asahi, A. Nagoya and G. Kresse, *Phys. Rev. B: Condens. Matter Mater. Phys.*, 2009, **79**, 115126.
- 12 M. Quintero, J. Marquina, E. Quintero, E. Moreno, S. Álvarez, C. Rincón, P. Grima, P. Bocaranda, D. Rivero, J. A. Henao and M. A. Macías, *Rev. Mex. Fis.*, 2014, **60**, 168–175.
- 13 W.-C. Yang, C. K. Miskin, N. J. Carter, R. Agrawal and E. A. Stach, *Chem. Mater.*, 2014, **26**, 6955–6962.
- 14 Y. Zhao and C. Burda, *Energy Environ. Sci.*, 2012, **5**, 5564–5576.
- 15 J. Perelaer and U. S. Schubert, *J. Mater. Res.*, 2013, **28**, 564–573.
- 16 F.-J. Fan, L. Wu and S.-H. Yu, *Energy Environ. Sci.*, 2013, **7**, 190–208.
- 17 J. J. Scragg, *Copper Zinc Tin Sulfide Thin Films for Photovoltaics: Synthesis and Characterisation by Electrochemical Methods*, Springer, 2011.
- 18 Q. Guo, J. V. Caspar, K. E. Roelofs, S. Subramoney and H. D. Rosenfeld, *Chem. Mater.*, 2014, **26**, 5664–5674.
- 19 M. Haderlein, D. Segets, M. Gröschel, L. Pflug, G. Leugering and W. Peukert, *Chem. Eng. J.*, 2015, **260**, 706–715.
- 20 H.-C. Schwarzer, F. Schwertfirm, M. Manhart, H.-J. Schmid and W. Peukert, *Chem. Eng. Sci.*, 2006, **61**, 167–181.

- 21 T. Milek and D. Zahn, *Nano Lett.*, 2014, **14**, 4913–4917.
- 22 D. Segets, M. A. J. Hartig, J. Gradl and W. Peukert, *Chem. Eng. Sci.*, 2012, **70**, 4–13.
- 23 M. A. J. Hartig, N. Jacobsen and W. Peukert, *Chem. Eng. Sci.*, 2014, **109**, 158–170.
- 24 S. Delbos, *EPJ Photovoltaics*, 2012, **3**, 13.
- 25 J. J. Scragg, P. J. Dale, D. Colombara and L. M. Peter, *ChemPhysChem*, 2012, **13**, 3035–3046.
- 26 E. A. Lund and M. A. Scarpulla, *Modeling Cu₂ZnSnS₄ (CZTS) solar cells with kesterite and stannite phase variation*, 2013, vol. 8620, p. 862015.
- 27 S. Chen, A. Walsh, X.-G. Gong and S.-H. Wei, *Adv. Mater.*, 2013, **25**, 1522–1539.
- 28 T. Maeda, S. Nakamura and T. Wada, *Jpn. J. Appl. Phys.*, 2011, **50**, 04DP07.
- 29 Q. Luo, Y. Zeng, L. Chen and C. Ma, *Chem. – Asian J.*, 2014, **9**, 2309–2316.
- 30 J. M. R. Tan, Y. H. Lee, S. Pedireddy, T. Baikie, X. Y. Ling and L. H. Wong, *J. Am. Chem. Soc.*, 2014, **136**, 6684–6692.
- 31 W. Wang, M. T. Winkler, O. Gunawan, T. Gokmen, T. K. Todorov, Y. Zhu and D. B. Mitzi, *Adv. Energy Mater.*, 2014, **4**, 1301465.
- 32 P. An, Z. Liang, X. Xu, X. Wang, H. Jin, N. Wang, J. Wang and F. Zhu, *RSC Adv.*, 2014, **5**, 6879–6885.
- 33 A. D. Collord and H. W. Hillhouse, *Chem. Mater.*, 2015, **27**, 1855–1862.
- 34 A. Pateter, W. Haas, B. Chernev, B. Kunert, R. Resel, F. Hofer, G. Trimmel and T. Rath, *Mater. Chem. Phys.*, 2015, **149–150**, 94–98.
- 35 R. Ahmad, M. Distaso, H. Azimi, C. J. Brabec and W. Peukert, *J. Nanopart. Res.*, 2013, **15**, 1–16.
- 36 M. Distaso, D. Segets, R. Wernet, R. K. Taylor and W. Peukert, *Nanoscale*, 2012, **4**, 864–873.
- 37 S. C. Riha, B. A. Parkinson and A. L. Prieto, *J. Am. Chem. Soc.*, 2009, **131**, 12054–12055.
- 38 Q. Guo, H. W. Hillhouse and R. Agrawal, *J. Am. Chem. Soc.*, 2009, **131**, 11672–11673.
- 39 T. Rath, W. Haas, A. Pein, R. Saf, E. Maier, B. Kunert, F. Hofer, R. Resel and G. Trimmel, *Sol. Energy Mater. Sol. Cells*, 2012, **101**, 87–94.
- 40 M. Kruszynska, H. Borchert, J. Parisi and J. Kolny-Olesiak, *J. Nanopart. Res.*, 2011, **13**, 5815–5824.
- 41 Y. Zhao, H. Pan, Y. Lou, X. Qiu, J. Zhu and C. Burda, *J. Am. Chem. Soc.*, 2009, **131**, 4253–4261.
- 42 H. T. Evans, *Science*, 1979, **203**, 356–358.
- 43 U. K. Gautam and B. Mukherjee, *Bull. Mater. Sci.*, 2006, **29**, 1–5.
- 44 M. Brandl, R. Ahmad, M. Distaso, H. Azimi, Y. Hou, W. Peukert, C. J. Brabec and R. Hock, *Thin Solid Films*, 2015, **582**, 269–271.
- 45 F. D. Benedetto, D. Borrini, A. Caneschi, G. Fornaciai, M. Innocenti, A. Lavacchi, C. A. Massa, G. Montegrossi, W. Oberhauser, L. A. Pardi and M. Romanelli, *Phys. Chem. Miner.*, 2011, **38**, 483–490.
- 46 N. C. Popa, *J. Appl. Crystallogr.*, 1998, **31**, 176–180.
- 47 P. Villars, K. Cenzual, J. Daams, R. Gladyshevskii, O. Shcherban, V. Dubenskyy, N. Melnichenko-Koblyuk, O. Pavlyuk, S. Stoiko and L. Sysa, in *Structure Types. Part 3: Space Groups (194) P63/mmc - (190) P6̄2c*, ed. P. Villars and K. Cenzual, Springer Berlin Heidelberg, 2006, p. 1.
- 48 M. Posfai and P. R. Buseck, *Am. Mineral.*, 1994, **79**, 308–315.
- 49 A.-J. Cheng, M. Manno, A. Khare, C. Leighton, S. A. Campbell and E. S. Aydil, *J. Vac. Sci. Technol., A*, 2011, **29**, 051203.
- 50 X. Fontané, L. Calvo-Barrio, V. Izquierdo-Roca, E. Saucedo, A. Pérez-Rodríguez, J. R. Morante, D. M. Berg, P. J. Dale and S. Siebentritt, *Appl. Phys. Lett.*, 2011, **98**, 181905.
- 51 P. A. Fernandes, P. M. P. Salomé and A. F. da Cunha, *J. Phys. D: Appl. Phys.*, 2010, **43**, 215403.
- 52 R. A. Wibowo, H. Yoo, A. Hölzing, R. Lechner, S. Jost, J. Palm, M. Gowtham, B. Louis and R. Hock, *Thin Solid Films*, 2013, **535**, 57–61.
- 53 M. Dimitrievska, A. Fairbrother, X. Fontané, T. Jawhari, V. Izquierdo-Roca, E. Saucedo and A. Pérez-Rodríguez, *Appl. Phys. Lett.*, 2014, **104**, 021901.
- 54 M. Böhm, G. Huber, A. MacKinnon, A. Scharmann and E.-G. Scharmer, *Physics of Ternary Compounds/Physik Der Ternären Verbindungen*, Springer Science & Business Media, 1985.
- 55 Y.-X. Wang, M. Wei, F.-J. Fan, T.-T. Zhuang, L. Wu, S.-H. Yu and C.-F. Zhu, *Chem. Mater.*, 2014, **26**, 5492–5498.
- 56 F. M. Doyle, R. Woods and E. S. I. E. and E. E. Division, *Electrochemistry in Mineral and Metal Processing VI: Proceedings of the International Symposium*, The Electrochemical Society, 2003.